International Journal of Technology 13(1) 190-201 (2022)
Received May 2021 / Revised July 2021 / Accepted July 2021

International Journal of Technology

http://ijtech.eng.ui.ac.id

Numerical Analysis of Floatplane Porpoising Instability in Calm Water During Takeoff

Muhammad Hafiz Nurwahyu Aliffrananda[1], Aries Sulisetyono[1*], Yuda Apri Hermawan[1], Achmad Zubaydi[1]

[1]*Department of Naval Architecture, Institut Teknologi Sepuluh Nopember, Surabaya 60111, Indonesia*

Abstract. In the operation of floatplanes, porpoising must be avoided, but it is a common occurrence during takeoff, as it induces longitudinal instability and compromises the safety and comfort of passengers. The mechanism of porpoising and the factors or variables that influence the occurrence of this phenomenon are explored in this study. Based on a review of the literature, the position of the longitudinal center of gravity (LCG) and the deadrise angle were found to be the two most significant variables affecting the porpoising phenomenon. The mechanism of porpoising was simulated using a numerical model based on computational fluid dynamics (CFD). The simulation findings were then compared to the results of a related model's towing tank experiment. With five velocity differences, a validated computational model was used to analyze the impact of LCG ordinates and deadrise angles on the frequency of porpoising. Compared to the LCG 50% length overall (LOA) configuration, the floater with an LCG 53% LOA configuration caused a higher heave porpoising amplitude by 4% for the floater with a 10° deadrise angle and 1% for the floater with a 20° deadrise angle at all speed variations. However, the pitch porpoising amplitude produced by the floater with an LCG 53% LOA configuration was found to be 4% higher than the LCG 50% LOA configuration for the floater with a 10° deadrise angle and -1% higher than the LCG 50% LOA configuration for the floater with a 20° deadrise angle. The results showed that the higher heave and pitch porpoising amplitude was generated by a low deadrise angle and a shift in the floater's center of gravity toward the bow.

Keywords: CFD; Deadrise; Floatplane; Porpoising; Take-off

1. Introduction

Seaplanes can operate on both land and water, making them suitable for short-distance travel (Xiao et al., 2020). and operations near coastal lines to reduce traffic at municipal airports while improving connectivity between secluded islands (Ito et al., 2016). Except for specific operations and restricted areas, seaplanes have been widely overlooked in modern aviation. Nonetheless, this aircraft model has begun to regain its appeal due to the robust advancements in computational abilities (Ito et al., 2016). Floatplanes, which are an amphibious type of seaplane, are equipped with submerged floats or pontoons underneath their fuselage. A numerical study in 2020 analyzed the optimal separation ratio (S/L) configuration of a catamaran hull design most suitable for the N219 floatplane by implementing a sailfish's hydrodynamic qualities to minimize the total hull resistance

*Corresponding author's email: sulisea@na.its.ac.id, Tel.: +62-31-5947254, Fax.: +61-31-5964182
doi: 10.14716/ijtech.v13i1.4903

caused by hull interference (Yanuar et al., 2020). This interference is also caused by changes in pressure and flow velocity around the catamaran hulls, which are affected by the form factor (Utama et al., 2021). This has been proven in a numerical study that aimed to clarify the reduced total resistance in a traditional catamaran by modifying the hull form in line with the Lackenby method (Iqbal and Samuel, 2017). The floats or pontoon's purpose is to provide lift force; any inconsistencies in the lift force led to dynamic instabilities, such as porpoising. The porpoising phenomenon, a rhythmical pitching motion on amphibious vessels equivalent to a swinging sensation (Gudmundsson, 2013), is commonly experienced by floatplanes during takeoff (Aliffrananda and Sulisetyono, 2021). Operability problems, such as increased takeoff time and track length (Gudmundsson, 2013), incidents during takeoff (Federal Aviation Administration [FAA], 2004), inconvenience to pilots and passengers (Faltinsen, 2005), and damage to the floater's construction (Abrate, 2011), are outcomes of porpoising. A deeper understanding of the complexity of these problems is required to determine methods that can minimize their occurrence.

The risk of porpoising was evaluated in a towing tank using high-speed craft models and two variations of deadrise angles (Day and Haag, 1952). A higher deadrise angle led to an increase in the critical trim, while a higher speed led to a decrease. The results were plotted to represent the longitudinal stability limits induced by different deadrise angles (Savitsky, 1964). In 1999, a program was developed to predict the porpoising instability induced by various deadrise angles, and the longitudinal center of gravity (LCG) (Sulisetyono, 1999) was validated against previous experiments (Day and Haag, 1952). A similar experiment conducted on a speed range of 3–15 m/s found that porpoising began to occur at 5 m/s, with the period decreasing over the increase in speed. The highest porpoising period occurred at 5 m/s while the lowest began at 15 m/s (Katayama, 2004). Another experiment on stepped and regular hulls (Sajedi and Ghadimi, 2020) found that the stepped hull decreased the average of the ship's heave and pitch motion and the porpoising amplitude. At high speeds, the start of porpoising was delayed on the ship with a stepped hull while at the same Froude number, the ship with a regular hull had begun porpoising (Sajedi and Ghadimi, 2020).

A numerical simulation of porpoising in a large seaplane model (Duan et al., 2019) concluded that the porpoising amplitude started to increase over time. Another similar numerical study was done on a modified N219 aircraft turned into a floatplane with a catamaran hull configuration, and the variations in LCG and deadrise angle were investigated to analyze the effects of LCG and deadrise angle on porpoising (Aliffrananda and Sulisetyono, 2021). The results were compared to a high-speed craft motion experiment (Sajedi and Ghadimi, 2020). A low deadrise angle generated a higher lift force, causing the floater to experience heave faster than other floater models with higher deadrise values. However, the LCG increased the heave and pitch period during porpoising if the LCG was near the stern of the floater (Aliffrananda and Sulisetyono, 2021). From these studies (Duan et al., 2019; Aliffrananda and Sulisetyono, 2021), the conclusion that amplification will continue to happen due to porpoising oscillation if the plane's position remains uncorrected can be drawn. Despite previous studies on porpoising, studies of its occurrence in floatplanes are still scarce. This paper addresses this research gap by engaging in further analysis of the porpoising phenomenon in floatplanes. The purpose of the analysis is to determine the optimal configuration of both LCG coordinates and the deadrise angle of floaters to mitigate the porpoising phenomenon. This phenomenon was simulated by utilizing computational fluid dynamics (CFD), variations of five traveling speeds, two LCG coordinates, and two deadrise angle variations.

2. Methods

2.1. Floater Model Description

The CFD simulation was only carried out on floater models with a range of takeoff speeds (Fn = 0.9 – 2.3) in a calm water and calm wind condition. The variations in this study included two deadrise angles of 10° and 20° as seen in Figure 1, two LCG variations of 50% (trim by stern) and 53% (even keel) of the floater's length overall (LOA), and two degrees of freedom (heave and pitch motion). Each floater was simulated based on a catamaran configuration, which was modeled and tested simultaneously. The 10° deadrise angle lowered the bottom hull to the baseline and increased the submerged area and the floater's displacement in return. Different LCG locations also generated trims during the initial condition of the floater.

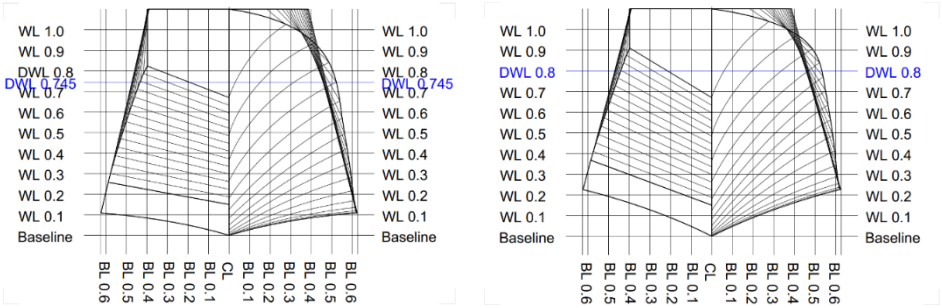

Figure 1 Comparison of floaters' body plans with different deadrise angles at: (a) 10°; and (b) 20°

Table 1 Main dimensions of the floaters

Hull Model		Floater 1	Floater 2
Length overall (LOA)	m	9.600	9.600
Length between perpendicular (LPP)	m	9.448	9.389
Length of waterline (LWL)	m	9.448	9.389
Breadth of demihull (B)	m	1.248	1.248
Height (H)	m	1.100	1.100
Draught (T)	m	0.800	0.745
Space between demihull	m	3.950	3.950
Forebody length (Lf)	m	5.400	5.400
Afterbody length (La)	m	4.200	4.200
Deadrise angle	°	20	10
Wetted surface area (WSA)	m^2	32.676	32.884
Displacement (Δ)	ton	7.664	7.630

A draft adjustment of the floater with a 10° deadrise angle was made to maintain a similar volume and displacement in both floaters. The corrected draft was 0.745 m compared to the draft of the 20° deadrise model, which was 0.8 m. The complete main dimensions of both floaters are listed in Table 1.

2.2. Mathematical Model

The incompressible unsteady Reynolds-averaged Navier Stokes (RANS) equations were used by the CFD flow solver while the turbulence was solved by the $k-\omega$ model. The spatial discretization of the transport equations was built using the finite volume method. The face-based approach uses unstructured three-dimensional meshes with an arbitrary number of constitutive faces to define non-overlapping control volumes. The velocity field was calculated using momentum conservation equations, and the pressure field was calculated using the mass conservation or continuity equation converted into a pressure equation (Versteeg et al., 1995). Additional transport equations were solved in the same way as momentum equations in turbulent flows, as well as discretized and solved using the

same principles. The mass and momentum equations shown in Equations 1 and 2 show v as flow velocity, ∇ as mass transport, ρ as fluid density, μ as viscous stress, f as external force, and t as time.

$$\frac{\partial \rho}{\partial t} + \nabla(\rho u) = 0 \tag{1}$$

$$\rho\left(\frac{\delta V}{\delta t} + v.\nabla v\right) = -\nabla p + \mu\nabla^2 v + f \tag{2}$$

2.2.1. k-ω turbulence model

The modeling of the turbulence effects in near-wall flow was conducted by means of RANS-based Wilcox's $k-\omega$ model (Wilcox, 1993). The model has been shown to be more numerically stable than the $k-\varepsilon$ model, particularly in the viscous sublayer near the wall. Due to the high values of ω in the wall regions, this model does not require explicit wall-damping functions like the $k-\varepsilon$ model and other two-equation models. The distance from the wall to the first point off the wall must be defined in numerical wall boundary conditions. The $k-\omega$ turbulence scale's transport model equations are described below.

$$\frac{\partial \rho K}{\partial t} + \frac{\partial}{\partial x_j}\left(\rho U_j K - (\mu + \sigma^* \mu_t)\frac{\partial K}{\partial x_j}\right) = \tau_{tij} S_{ij} - \beta^* \rho \omega K \tag{3}$$

$$\frac{\partial \rho \omega}{\partial t} + \frac{\partial}{\partial x_j}\left(\rho U_j \omega - (\mu + \sigma \mu_t)\frac{\partial \omega}{\partial x_j}\right) = \alpha \frac{\omega}{K}\tau_{tij} S_{ij} - \beta \rho \omega^2 \tag{4}$$

where $\alpha = {}^{5}/_{9}$, $\beta = {}^{3}/_{40}$, $\beta^* = {}^{9}/_{100}$, $\sigma = 0.5$, and $\sigma^* = 0.5$ according to Wilcox (1993).

2.3. Numerical Modeling

2.3.1. Computational domain

The computational domain in this analysis utilized a free surface mode to accurately depict a towing tank simulation. Boundaries such as the top, side walls, and bottom were set as no-slip walls in addition to the floater. It is crucial for the size of the domain to be large enough to avoid compromising the simulation results.

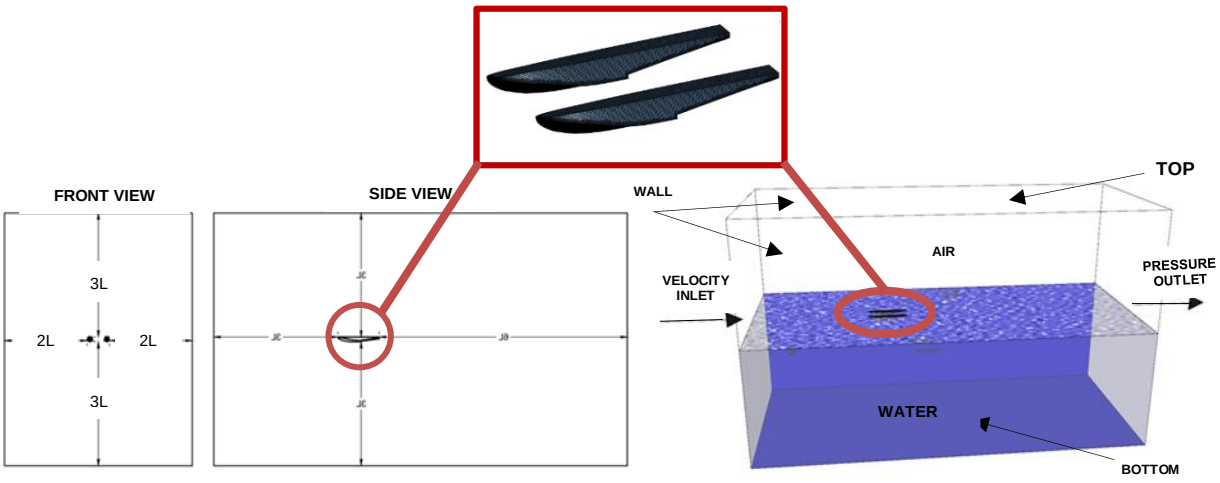

Figure 2 (a) Computational domain; and (b) boundary condition used for the CFD simulation

Based on these considerations, the configuration of the domain used in this study was two to three times larger than the recommendation issued by the ITTC (2011) as a means of providing more room for the floater to move freely in two degrees of freedom, specifically the heave and pitch motions. The domain size was a function of the floater's overall length, represented by L, as shown in Figure 2. The velocity inlet was placed 3 L from the forward

end of the floater while the pressure outlet was placed 6 L from the rear end. The extended domain at the rear end of the floater was determined to capture the outline of the water surface generated at the back of the floater during movement.

2.3.2. Computational grid

Smooth mesh around the floater's wall region was generated by setting the inflation layer for an accurate representation of the flow around the area (Duan et al., 2019), which focused on hydrodynamic force as the main component in a net force that supports the floater during high-speed operation.

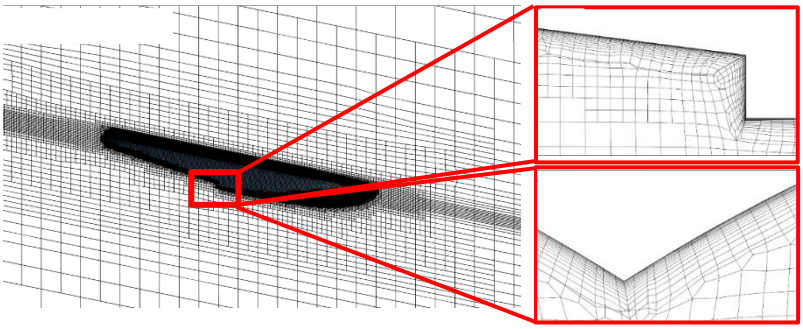

Figure 3 Grid generation by using an inflation layer near the floater wall and by generating denser mesh in the free surface area to accurately model the fluid flow around the floater

Another important outome of the modeling is the fluid flow occurring in the free surface area behind the floater obtained by mesh refinement around the free surface (Figure 3). The outer region was left unrefined to save computational memory and shorten computational time, as these values were not further analyzed. However, the grid around this region was created by a structured hexahedral mesh to minimize computational effort over the large computational domain. A mesh deformation method, as seen in Figure 4, was adopted to accommodate the heave and pitch motion, allowing the grid's structure to bend when following the movement of the floater without being damaged or torn. This challenge was also overcome by increasing the domain size to better accommodate the floater's movements (Vanherzeele, 2015). The figure shows mesh deformation in 1 s intervals between 2.5–3.5 s of simulation time.

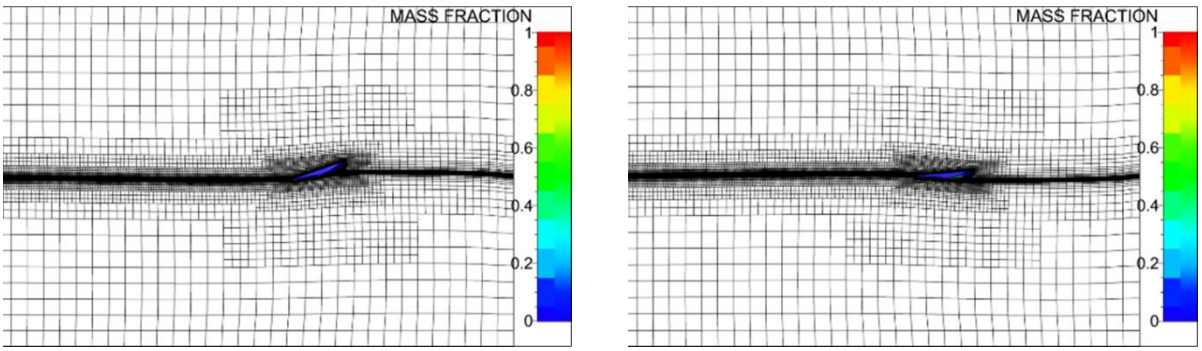

t = 2.5 s t = 3.5 s

Figure 4 Mesh deformation method depicted in 1 s intervals

Following the determination of the computational domain and the generation of the computational grid, a grid independence study was conducted. This grid study was conducted to determine the optimal number of cells with the least effect on the computational results. The drag and lift forces of the floater were chosen as the parameters

to be monitored during this process. The result can be seen in Table 2, where F_D is drag force, F_L is lift force, and Δ denotes the deviation of a parameter obtained by a different number of cells.

Table 2 Result of grid independence study of the floaters

Total Number of Cells (×10⁶)	F_D (kN)	Δ F_D (%)	F_L (kN)	Δ F_L (%)
1.404	13.271		38.079	
1.871	13.157	0.86	43.888	15.26
3.361	12.518	4.86	36.552	16.72
5.448	12.098	3.35	33.340	8.79
7.265	11.942	1.30	33.340	0.00

From the table, the deviation between the total number of cells of 5.5 and 7.3 million reached below 2% for the drag force parameter and reached 0% for the lift force parameter. The maximum deviation between the total number of cells in the grid independence study should not exceed 5%. Therefore, from these results, the number of elements of 5.5 million was chosen to carry out the main simulation in this study.

2.3.3. Validation of numerical model

To ensure the credibility of the results obtained from the numerical modeling of the porpoising phenomenon, a validation study was first conducted beforehand using the US Navy Combatant DTMB 5415 ship model to be compared to an experimental study of the same ship conducted by ITTC (2014), to serve as the benchmark for the validation of CFD studies. The procedure for these experiments followed the ITTC Recommended Procedures and Guidelines (ITTC, 2011).

Table 3 Comparison of the monitored parameters between the ITTC experiment and CFD results

Speed (Fn)	Heave (mm)			Pitch (°)		
	CFD	ITTC	Δ (%)	CFD	ITTC	Δ (%)
0.100	-1.147	-1.050	9.28	-0.014	-0.013	7.25
0.280	-10.244	-10.210	0.33	-0.104	-0.104	0.12
0.410	-25.592	-25.340	0.99	0.379	0.379	0.07

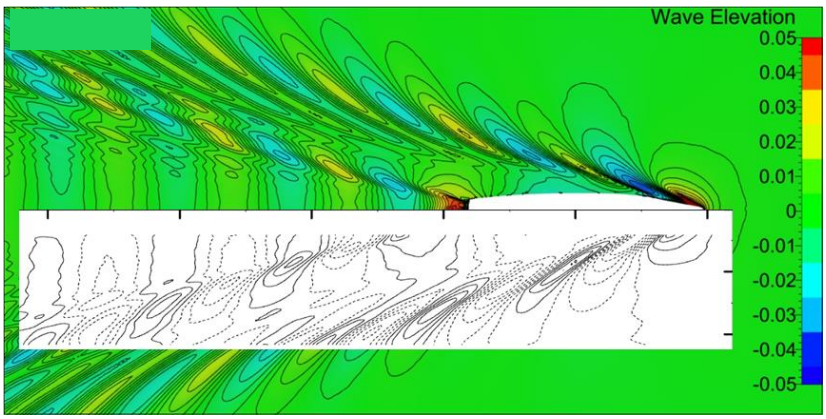

Figure 5 Comparison of wave patterns from the ITTC experiment and CFD simulation at Fr = 0.28

Table 3 shows the comparison of the CFD simulation results with the ITTC experimental results regarding the heave motion, pitch motion, and average deviation (Δ) between the CFD simulation and the experiment. This validation study was also conducted using the mesh deformation method to accommodate the heave and pitch motions. The heave motion parameter obtained an average deviation of 3.53% while the pitch motion

reached an average deviation of 2.48%. All parameters exhibited an average deviation value below 5%, indicating that the preprocessor and solver setups of the CFD had been done properly and were therefore suitable for use in the next simulation process. In addition to the heave and pitch motion validation, a comparison between the wave patterns of the CFD simulation and a similar experiment was conducted to show more confidence in the results. As can be seen in Figure 5, the wave pattern of the CFD simulation conformed well to the wave pattern formed by the DTMB 5415 that was observed in an experiment conducted in 2001 (Olivieri et al., 2001). Isolines represent these wave patterns by forming distinct lines to differentiate wave contours based on each of their specific wave heights along the surface, starting at the fore of the ship to the end of the simulation domain. Values larger than zero depict a peak of the wave, whereas values less than zero depict a trough. The wave heights are a good interpretation of the wave pattern in an easy-to-understand and realistic manner.

3. Results and Discussion

Due to the transient nature of the simulation, the obtained results were acquired as a function of time, causing the values to oscillate during the computational process. This oscillation centered at the Center of Gravity (CG) occurred following the motion of the floater. Therefore, the results presented in this study were taken from the average of the highest 50% of the motion amplitude, porpoising amplitude, and porpoising period values, where each simulation was conducted for 8 s. At a certain speed, the elevation value will always fluctuate without displaying any relatively stable values. Fluctuation means that the floater experiences instability in certain modes of operation. This instability is depicted as a fluctuating line in a graph, as opposed to stable motion values. When the up and down motion values are stable, the curve forms a straight line, indicating little to no change in motion. This is known as a stable planning condition.

The simulation results showed that the occurring instability led to a fluctuating and relatively uniform increase in elevation. The results conform well to the definition of porpoising, in which the occurrence of elevation is repetitive with almost the same amplitude. However, the increase in speed brought about an increase in the heave amplitude, where the deadrise angle and LCG also affected the elevation value. The motion at speeds of 9.295 m/s and 21.689 m/s (Froude Numbers 0.958 and 2.235) is depicted in Figure 6a and 6c. From Figure 6, the motion oscillation phenomenon started at the first second, where the floater was at the peak of the cycle and continued to move downwards at twice the amplitude of the porpoising. In addition, the amplitude of porpoising was found to increase over time. The deadrise angle of 10° was also found to generate a higher value in the elevation amplitude as opposed to the 20° variation. In other words, at the same LCG value, different deadrise angles induced a similar phase difference in movement. Similar to the heave, the rotation of the pitch motion as a function of time also experienced fluctuation at a certain velocity, as seen in Figure 6 and 6d. During the fluctuation, the values were found to be unsteady, as they did not share any relatively similar values. The pitch motion graph showed a straight line when the floater was stable. When the floater was unstable, a fluctuating line appeared on the motion graph, indicating significant fluctuations in rotational values. Porpoising is also defined as a pattern of pitch with identical amplitudes that occur repeatedly. The deadrise angle and the location of the LCG also affected the rotational value, as they affected the heave. This is due to both motion interplays, also known as the couple heave and pitch motions. Both motions are affected by the lift force and the time experienced by the floater.

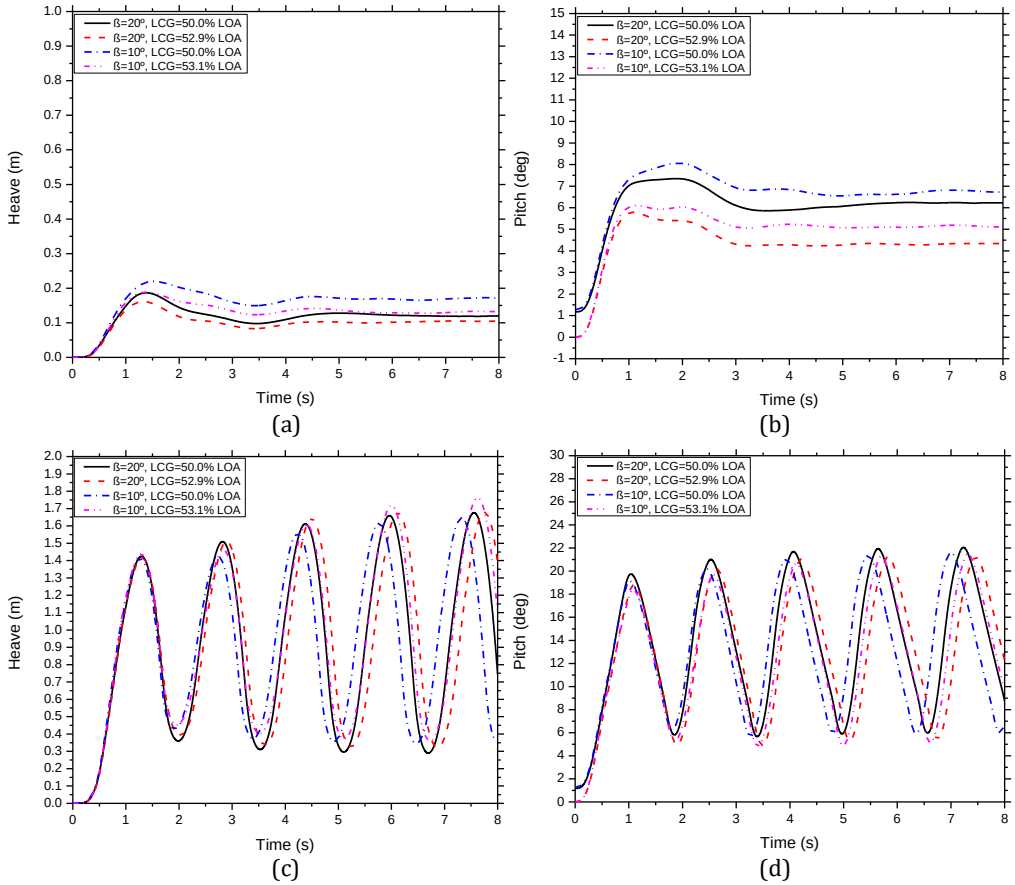

Figure 6 Motion of floaters as a function of time: (a) heave motion, and (b) pitch motion at 9.295 m/s; and (c) heave motion, and (d) pitch motion at 21.689 m/s

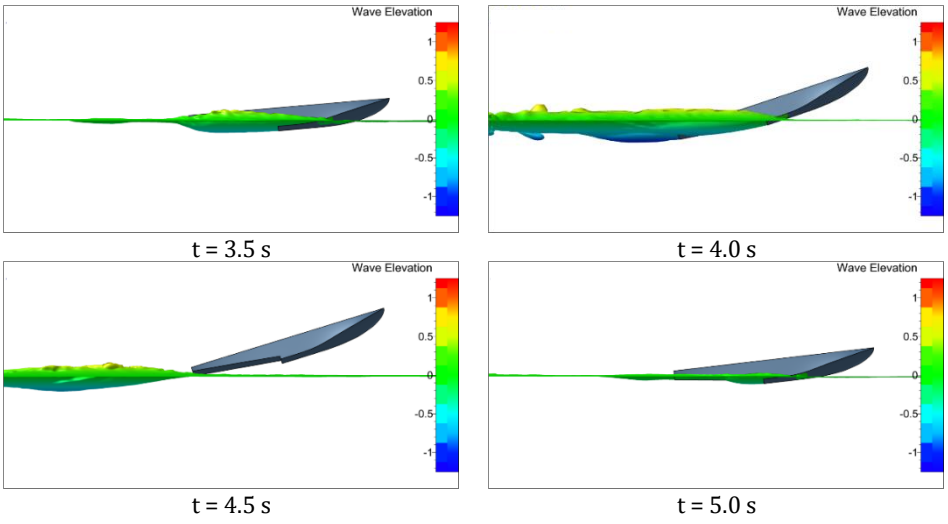

Figure 7 Heave and pitch motions of floaters with a deadrise angle of 20° and an LCG of 52.9% LOA on 21.689 m/s across the designated time period

A clear illustration of the motion during its porpoising phase at a speed of 21.689 m/s is provided by Figure 7. The illustration was taken at 0.5 s intervals and offers a side view that shows the floater's behavior in accordance with the time response shown in Figure 6. The leap at 4.5 s is represented by a peak value in the graph, as seen in Figure 6c, indicating that the heave motion was taking place, causing the floater to leap above the water.

However, the trough in Figure 6c at 5.0 s caused the floater to descend back into the water. This cycle will continue to repeat if the heave and pitch values of the floater are left unaltered. In addition, Figure 7 also shows the wave heights that occurred along the floater. In Figure 6d at 4.0 s, the pitch value reached its peak, which caused the stern of the floater to generate a wave as it became more submerged in the water.

3.1. Heave and Pitch Motion Amplitude on the Floaters

Figure 8a and 8b shows the behavior of the heave and pitch motion amplitudes as a function of speed. With $Fn < 1$, the floater at a deadrise angle of 20° and an LCG location of 52.9% LOA generated the smallest average heave and pitch motion amplitude, respectively. However, the largest heave and pitch motion amplitude at the same velocity was generated by the floater with a deadrise angle of 10° and an LCG position of 50% LOA. At the highest speed, the lowest heave amplitude was found on the floater with a deadrise angle of 10° and an LCG of 50% LOA, while the lowest pitch motion amplitude was found at the same deadrise angle and an LCG of 53.1% LOA. Still at the highest speed, the highest heave amplitude occurred at the same deadrise angle, with an LCG of 53.1% LOA, while the highest pitch amplitude was induced by the deadrise angle of 20° and an LCG 50% LOA configuration.

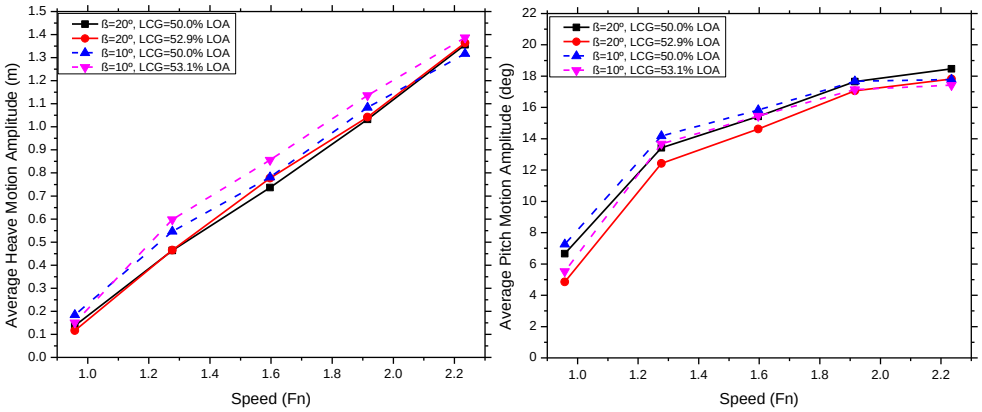

Figure 8 Effect of LCG and deadrise angle variation on: (a) heave motion; and (b) pitch motion amplitude

A smaller deadrise angle resulted in a higher lift force, meaning that the deadrise angle has an impact on the floater's heave and pitch motion amplitudes at any given speed. In addition, the CG located closer to the bow provided a higher heave and pitch amplitude than the other CG configurations. Near the stern, CG allowed the floater's initial position to be trimmed by the stern, making it easier to rotate counterclockwise. $Fn < 1$ generated a smaller heave and pitch amplitude of all variations of CG near the bow while at $Fn > 1$, the CG near the bow induced a higher heave and pitch amplitude.

3.2. Heave and Pitch Porpoising Amplitudes on Floaters

During the increase in speed, the porpoising amplitude experienced by the floater increased. At 15.492 m/s, the smallest heave porpoising amplitude occurred at the floater with a deadrise angle of 20° and LCG of 50% LOA, while the smallest pitch porpoising amplitude was generated by the same deadrise angle and an LCG of 52.9% LOA, respectively. At the same speed, the largest heave porpoising amplitude occurred at the deadrise angle of 10° and an LCG of 53.1% LOA while the largest pitch porpoising amplitude was attained by the same configuration. At 21.689 m/s, the smallest heave porpoising amplitude occurred on the floater with a deadrise angle of 10° with an LCG of 50% LOA,

while the smallest pitch porpoising amplitude was induced by the same LCG configuration but with a deadrise angle of 20°. However, the largest heave porpoising amplitude occurred at the deadrise angle of 20° at the same LCG location while the largest pitch porpoising was generated by the deadrise angle of 10° at the same LCG configuration.

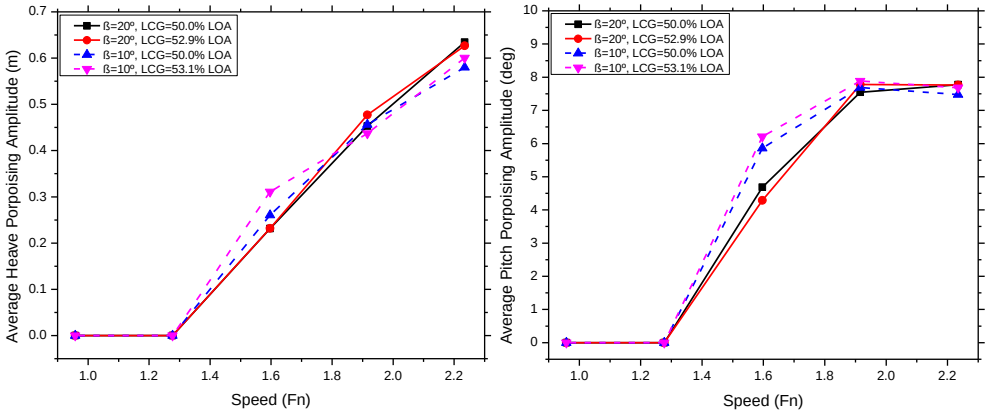

Figure 9 Effect of LCG and deadrise angle variation on: (a) heave porpoising; and (b) pitch porpoising (b) amplitude

The heave and pitch porpoising did not occur until $Fn > 1.3$, where the amplitudes increased over the increase in the operating speed. In Figure 9, the effects of LCG and the deadrise angle on heave and pitch porpoising are shown. The LCG near the bow of the floater increased the heave and pitch porpoising amplitudes. The effects of the deadrise angle can be seen at the highest simulation speed, where the deadrise angle of 20° induced higher heave and pitch porpoising amplitudes compared to the deadrise angle of 10°.

3.3. Heave and Pitch Porpoising Period on Floaters

Since heave porpoising did not occur until $Fn > 1.3$, the same condition applied to the heave porpoising period, as depicted by Figure 10a. At 15.492 m/s, the smallest heave porpoising period occurred on the floater with a deadrise angle of 10° and an LCG of 50% LOA while the smallest pitch porpoising period was generated by the same configuration. At the same speed, both the largest heave and pitch porpoising amplitudes occurred at the same deadrise angle of 10° and an LCG of 53.1% LOA, respectively.

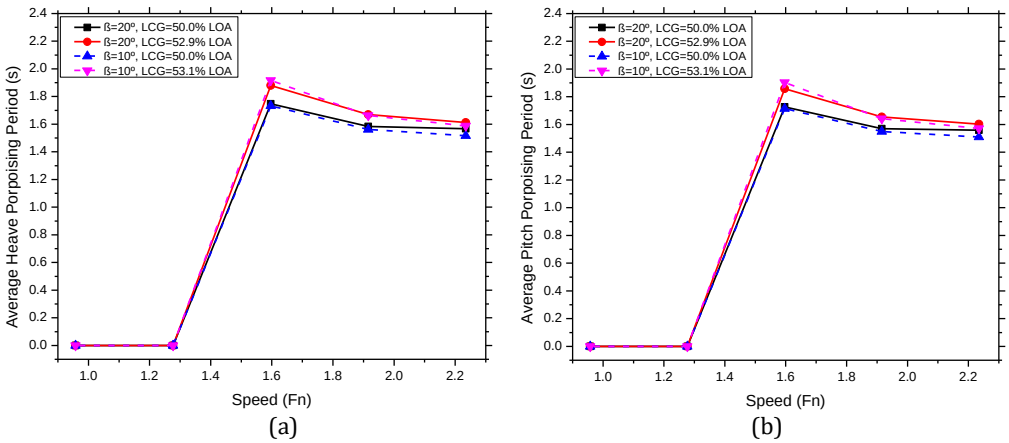

Figure 10 Effect of LCG and deadrise angle variation on the heave porpoising period

At the highest speed, the smallest heave porpoising period occurred on the floater with a deadrise angle of 10° and an LCG of 50% LOA while the smallest pitch porpoising period was generated by the same configuration. At the same speed, the largest heave porpoising period occurred at a deadrise angle of 20° and LCG of 52.9% LOA while the largest pitch porpoising period was obtained by the same configuration. As the operating speed increased, the heave and pitch porpoising periods decreased. The results conform well to the study conducted on towing tanks to elucidate the porpoising mechanism occurring in high-speed crafts. According to the study, the porpoising period was found to decrease as speed increased (Katayama, 2004). Figure 10 also highlights the effect that the LCG and deadrise angle had on the heave and pitch porpoising periods. As the LCG approached the floater's bow, the heave and pitch porpoising periods were found to increase. At the highest velocity, the deadrise angle of 10°, as opposed to the 20°, induced a higher heave and pitch porpoising period.

4. Conclusions

CFD has proven its ability to accurately simulate the porpoising phenomenon on the floaters of a floatplane during takeoff operations. High-speed fluid flows, as the focus of the simulations, were modeled using the unsteady flow RANS equation and the $k-\omega$ turbulence model. Structured hexahedral mesh and deformation mesh methods were utilized to accommodate the floater's motion. The numerical computational setup was validated against the ITTC experiment using the DTMB 5415 models. Based on the dynamic features imposed by the porpoising motion on the floater seen at various speeds, a few conclusions were obtained. First, at both deadrise angle variations, LCG near the floater's bow generated higher heave and pitch porpoising amplitudes. Second, the low deadrise angle gave rise to a higher heave and pitch porpoising amplitude. Finally, the porpoising periods for both motions followed the same pattern, with the values decreasing after reaching its peak. However, higher deadrise angles resulted in overall lower porpoising periods.

Acknowledgements

The authors would like to thank the National Research and Innovation Agency (BRIN) of Indonesia and the Institut Teknologi Sepuluh Nopember (ITS) for funding this study under the scheme of "Basic Research Awards" with contract number 3/AMD/E1/KP.PTNBH/2020.

References

Abrate, S., 2011. Hull Slamming: Applied Mechanics Reviews. *Applied Mechanics Reviews*, Volume 64(6), pp. 1–35

Aliffrananda, M.H., Sulisetyono, A., 2021. Porpoising Instability Study of the Floatplane during Takeoff Operation on Calm Water. *In:* IOP Conference Series Materials Science and Engineering, Volume 1052(1), pp. 1–15

Day, J.P., Haag, R.J., 1952. *Planing Boat Porpoising*. Thesis in Webb Institute of Naval Architecture, Glen Clove, New York

Duan, X., Sun, W., Chen, C., Wei, M., Yang, Y., 2019. Numerical Investigation of The Porpoising Motion of a Seaplane Planing on Water with High Speeds. *Aerospace Science and Technology*, Volume 84, pp. 980–994

Faltinsen, O.M., 2005. *Hydrodynamics of High-Speed Marine Vehicles*. Cambridge University Press, Cambridge, UK

Federal Aviation Administration, 2004. *Seaplane, Skiplane, and Float/Ski Equipped Helicopter Operations Handbook*. Aviation Supplies & Academics Inc, Newcastle, Washington, USA

Gudmundsson, S., 2013. *General Aviation Aircraft Design*. Elsevier Inc., Amsterdam, Netherlands

Iqbal, M., Samuel., 2017. Traditional Catamaran Hull Form Configurations that Reduce Total Resistance. *International Journal of Technology*, Volume 8(1), pp. 85–91

Ito, K., Dhaene, T., Sakurai, T., 2016. Longitudinal Stability Augmentation of Seaplanes in Planning. *Journal of Aircraft*, Volume 53(5), pp. 1332–1342

ITTC, 2011. ITTC-Recommended Procedures and Guidelines: Practical Guidelines for Ship CFD Application. *In:* International Towing Tank Conference. ITTC, Zürich, Switzerland

ITTC, 2014. Resistance Committee: Final Report and Recommendation to the 27th ITTC. *In*: 27th ITTC Conference. ITTC, Copenhagen, Denmark

Katayama, T., 2004. Mechanism of Porpoising Instabilities for High-Speed Planing Craft. *In:* Proceedings of the Sixth ISOPE Pacific/Asia Offshore Mechanics Symposium 2004, 12–16 September, Vladivostok, Russia, pp. 171–178

Olivieri, A., Pistani, F., Avanzini, A., Stern, F., Penna, R., 2001. Towing Tank Experiments of Resistance, Sinkage and Trim, Boundary Layer, Wake, and Free Surface Flow Around a Naval Combatant INSEAN 2340 Model. *IIHR Technical Report No 421*. IHRR-Hydroscience & Engineering, College of Engineering, The University of Iowa, Iowa City, Iowa

Sajedi, S.M., Ghadimi, P., 2020. Experimental and Numerical Investigation of Stepped Planing Hulls in Finding an Optimized Step Location and Analysis of Its Porpoising Phenomenon. *Mathematical Problem in Engineering*, Volume 1, pp. 1–18

Savitsky, D., 1964. Hydrodynamic Design of Planing Hulls. *Marine Technolgy SNAME N1*, Volume 1(4), pp. 71–95

Sulisetyono, A., 1999. *Computing Porpoising Instability and Motions of a High-speed Boat in Waves.* Master's Thesis, Graduate Program, Dalhousie University, Nova Scotia, Canada

Utama, I.K.A.P., Aryawan, W.D., Nasirudin, A., Sutiyo., Yanuar., 2021. Numerical Investigation into the Pressure and Flow Velocity Distributions of a Slender-Body Catamaran Due to Viscous Interference Effects. *International Journal of Technology*, Volume 12(1), pp. 149–162

Vanherzeele, A.J., 2015. NUMECA Customer Area: Users' Guide Overview. Available Online at http://portal.numeca.be/, Accessed on April 22, 2020

Versteeg, H., Malalasekera, W., Orsi, G., Ferziger, J.H., Date, A.W., Anderson, J.D., 1995. *An Introduction to Computational Fluid Dynamics: The Finite Volume Method: Second Edition*. McGraw-Hill, Pearson (2007), Upper Saddle River, United States

Wilcox, D.C., 1993. *Turbulence Modeling for CFD*. DCW Industries, Inc., La Cañada Flintridge, California, USA

Xiao, Q., Fan, L., Yapeng, L., 2020. Risk Assessment of Seaplane Operation Safety using Bayesian Network. *Symmetry*, Volume 12(6), pp. 888–907

Yanuar., Gunawan., Utomo, A.S.A., Luthfi, M.N., Baezal, M.A.B. Majid, F.R.S., Chairunisa, Z., 2020. Numerical and Experimental Analysis of Total Hull Resistance on Floating Catamaran Pontoon for N219 Seaplanes based on Biomimetics Design with Clearance Configuration. *International Journal of Technology*, Volume 11(7), pp. 1397–1405